

IMPLEMENTATION OF A SPHERICAL DOUBLE PLASMA-MIRROR TELESCOPE FOR A MULTI-PETAWATT LASER

V. SCUTELNIC,^{1,‡,*} M. SPEICHER,^{1,‡} A. FAZZINI,¹ P. GHENUCHE,² D. DORIA,² A. AILINCUTEI,³
B. GONZALEZ- IZQUIERDO,¹ T. ASAVEI,² S. BALASCUTA,² J.J. BEKX,¹ P.-G. BLEOTU,² G.
BODINI,¹ C. BRAGANZA,¹ A. F. BRODERSEN,¹ A. CAVALLI,¹ O. CHALUS,³ G. COJOCARU,³ J.
D'MELLO,¹ I. DANCUS,² C. DERYCKE,³ F. DEURVORST,¹ M. EHRLMANNTRAUT,¹ D.
GENGENBACH,¹ D.G. GHITA,² L. GIUFFRIDA,⁴ M. GUGIU,² M. M. GÜNTHER,¹ O. JUINA,¹ K.
KENNEY,¹ S. KUMAR,¹ M. MARTINEZ-PACHECO,¹ I. MINGUEZ BACHO,¹ S. NORBAEV,² N.
POETRANTO,¹ H. RUHL,¹ E. SCHORK,¹ M. STEIN,¹ S. STEINKE,^{1,¶} A.-M. TALPOSI,² A. TOMA,² M.
TOSCA,^{4,5} A. UBARHANDE,¹ L. VASESCU,² E. GAUL,¹ D. E. RIVAS,¹ M. S. SCHOLLMEIER^{1,1} AND
G. KORN¹

¹Marvel Fusion GmbH, Theresienhöhe 12, 80339 Munich, Germany

²Extreme Light Infrastructure (ELI-NP) & Horia Hulubei National Institute for R&D in Physics and
Nuclear Engineering (IFIN-HH), 30 Reactorului Street, 077125 Magurele, Romania

³Thales LAS France, 78990 Élancourt, France

⁴ELI Beamlines Facility, The Extreme Light Infrastructure ERIC, Dolní Brežany 252 41, Czech
Republic

⁵Charles University, Faculty of Mathematics and Physics, Department of Macromolecular Physics,
Prague 180 00, Czech Republic.

[‡]These authors contributed equally

[¶]Until June 2023.

*valeriu.scutelnic@marvellfusion.com

¹marius.schollmeier@marvellfusion.com

1. Simulation details

Physical Optics Propagation is used to simulate diffraction effects. For this, a coherent optical beam at the central wavelength of the laser (810 nm) is propagated through the optical system. A top hat beam type and 1024x1024 grid was used to sample the beam.

Standard spot diagrams are simulated by tracing bundles of rays through the optical system to the focal plane to show ray distributions. The Airy disk radius is calculated as 1.22 times the central wavelength of the laser multiplied by the F/# of the system.

The point spread function is computed using direct integration of the Huygens wavelets method, a grid of 256x256 pixels was used for sampling the pupil and image. The Strehl ratio is computed by dividing the peak intensity of the point spread function with and without considering aberrations. The wavelengths and their weight are chosen to reproduce the experimentally measured spectrum of the laser, the discretization step in the simulation is 5 nm.

Spherical, coma, astigmatism, field curvature, distortion, longitudinal and transversal color coefficients in the Seidel diagram are computed and displayed for each surface in the optical system.

2. Double-plasma mirror (DPM) optical system

2.1 Higher-order reflections on the plasma mirrors

During alignment the laser intensity is low and the front surfaces of the plasma mirrors are highly transmissive, leading to multiple reflections from the back surfaces that are also directed towards the main focal plane. Figure S1 depicts the result of a non-sequential ray tracing simulation, where rays after each reflection are represented with a different color. To ensure all these reflections have negligible intensity on target, we use AR coating on both front and back surfaces of the mirrors.

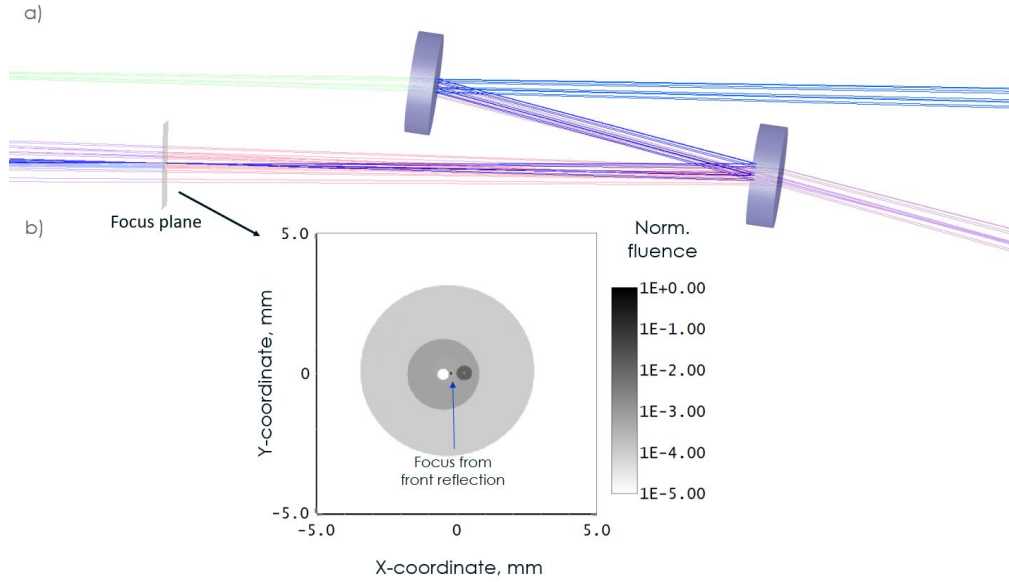


Figure S1. (a) Rays originating from reflections at front surfaces of the plasma mirrors are shown in bright blue color. Reflections involving the back surfaces are shown in faint colors. (b) Intensity distribution at the focal plane. The fluence distribution of reflections involving back surfaces is >2 orders of magnitude lower than for the main focus before the plasma mirror is triggered.

2.2 Laser intensity on plasma mirrors

The simulated intensity on the plasma mirrors for a pulse power of 10 PW is shown in Figures S2 and S3.

The full width at half maximum (FWHM) of the beam on PM1 measures 2.6 mm in diameter.

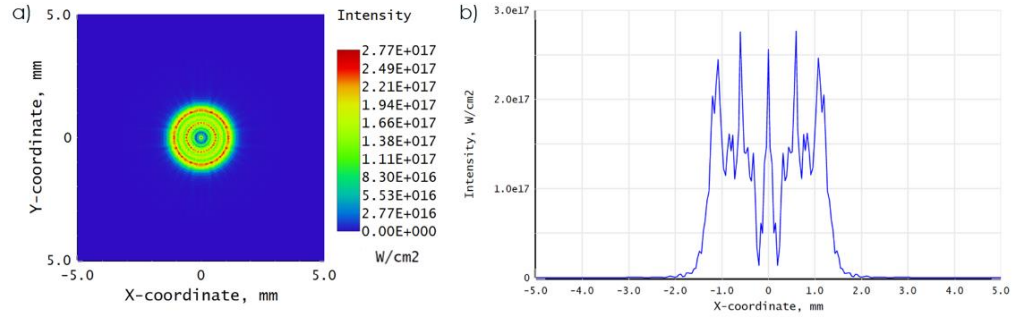


Figure S2. Beam profile on PM1. (a) 2-D intensity map. (b) Line-out across the center-axis for the intensity profile.

The FWHM of the beam on PM2 measures 3.4 mm in diameter (see Figure S3). An average reflectivity of PM1 equal to square root of total DPM reflectivity $\sqrt{0.68}$ is used in the simulation.

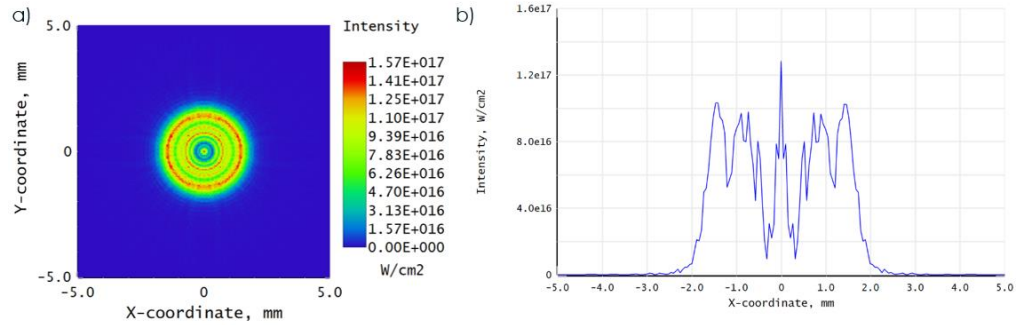


Figure S3. Beam profile on PM2. (a) 2-D intensity map. (b) Line-out across the center-axis for the intensity profile.

2.3 Laser contrast measurement

The laser contrast is measured with a third order autocorrelator (TUNDRA, Ultrafast Innovations) and is shown in Figure S4. The contrast is below 10^{-7} up to -5 ps. The inherent background of this device is 10^{-9} , limiting the dynamic range. Nonetheless, a 10^{-11} contrast could be measured for delays before -100 ps [1].

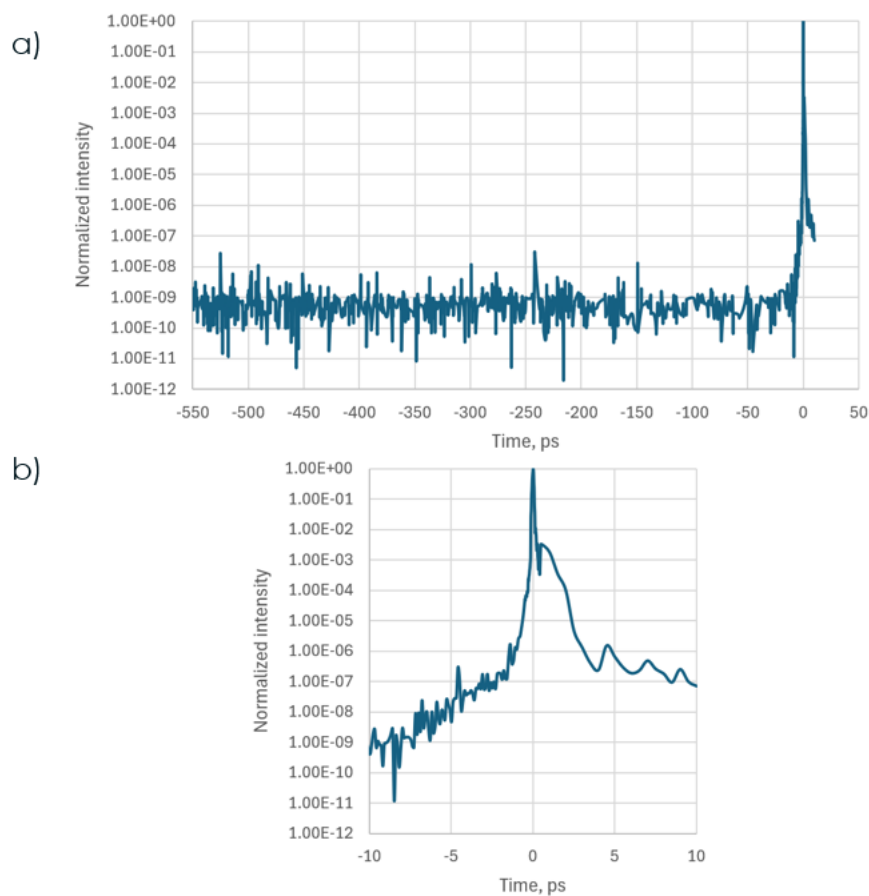


Figure S4. Picosecond contrast measurement with Tundra: (a) full range, (b) zoom on the onset of the intensity rise.

2.4 Correction of the residual astigmatism with the deformable mirror

To remove the residual aberrations, the deformable mirror (DM), installed before the compressor, can be adjusted (Figure S5). In this way, a diffraction limited focus can be obtained by changing the Z_2^2 – vertical astigmatism Zernike term. Actuation of the DM motors is in the range of ± 210 nm, which is well within the range of commercial DMs. The value of the theoretically predicted flexing of DM has been found to be consistent with the experiment.

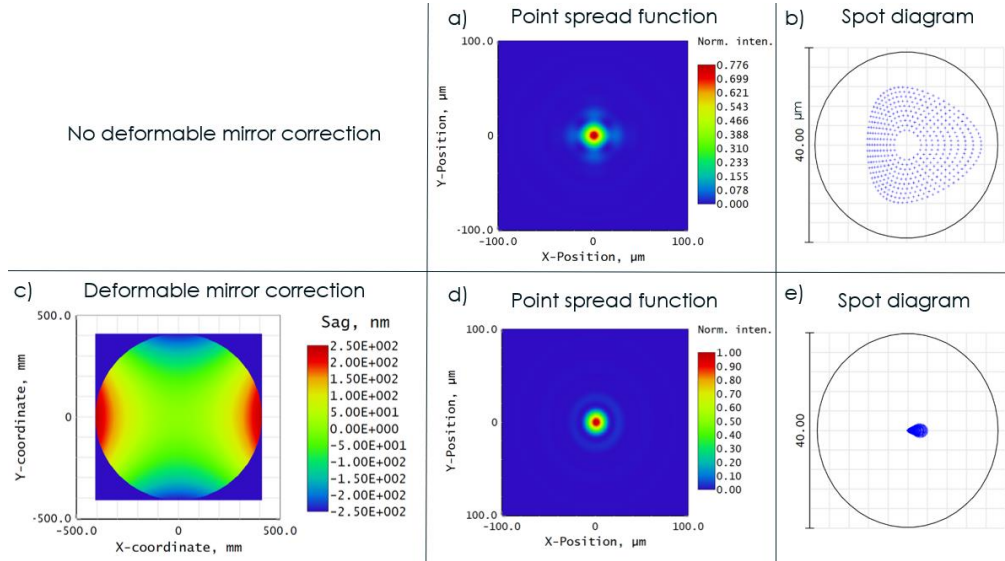


Figure S5. No deformable mirror correction: (a) Point spread function (Strehl ratio 0.776) and (b) spot diagram. Correction with the deformable mirror results in a diffraction limited focus: (c) Sag of the deformable mirror, (d) focus point spread function (Strehl ratio 0.998) and (e) spot diagram.

The wavefront map and phase map at the focal plane (Figure S6) provide a deeper insight into the role of the deformable mirror correction. The phase has been computed by means of Physical Optics Propagation.

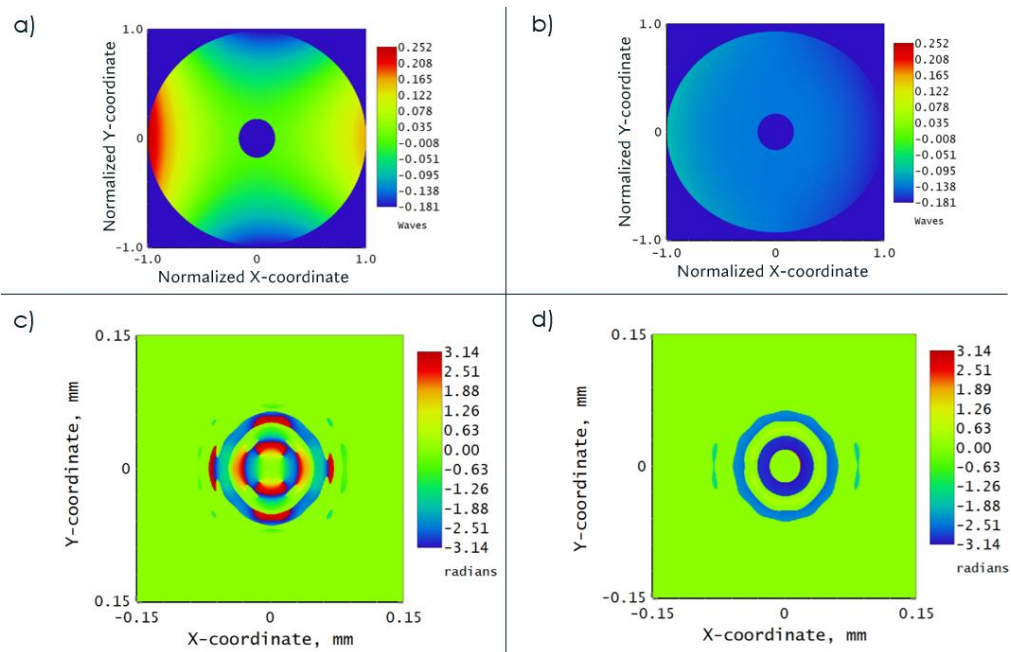


Figure S6. (a) Wavefront map at the focal plane based on ray tracing before and (b) after adjusting the deformable mirror. (c) Phase at the focal plane before and (d) after adjusting the deformable mirror.

2.5 Tunability of F/#

By changing the distance between plasma mirror 2 and F/19.4 focal plane a variable F/# of the system, and hence a variable focus size, can be achieved. The distance between the F/63.5 focus and PM1 needs to be adjusted as well to produce a sharp focus. In Figure S6 the point spread function is shown for the DPM system variations, illustrating the facile tunability of the focus intensity. The intensity stops growing with the decrease to F/16 because the accumulated aberrations reduce significantly the Strehl ratio, however in this case the focus can still be optimized further by a moderate correction in the deformable mirror, similarly as in Figure S5.

The experimentally measured distance between PM2 and the demagnified focus is 73 ± 0.5 mm, this leads to the F/# uncertainty of 19.4 ± 0.6 .

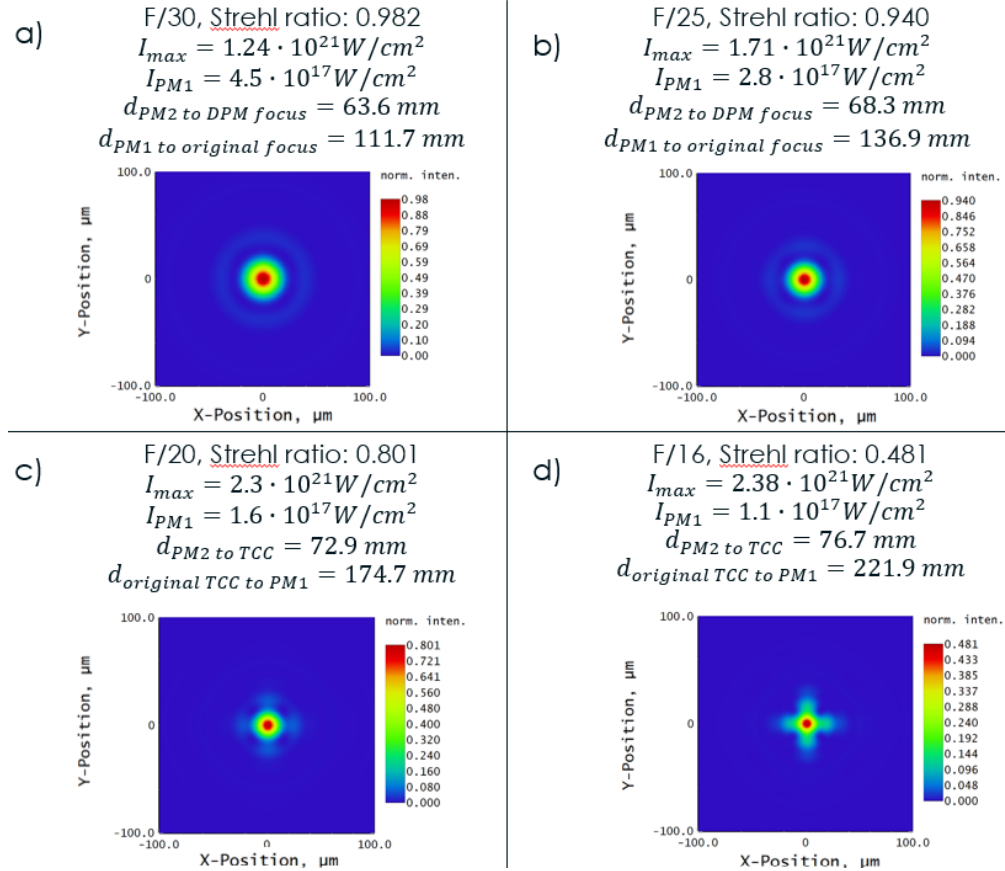


Figure S7. Calculation of the point spread function (PSF) and Strehl ratio for various distances between the plasma mirror 2 and the target chamber center. The distance from plasma mirror 1 to the original focal plane has been optimized. The intensity is calculated assuming no loss of laser energy on the mirrors and 10 PW pulses.

2.6 Micrographs of PM ablation and material deposition

PM1 and PM2 have a second large damage spot that is two times bigger than the primary damage spot (see Figure S8 and S9 for a representative case of damage on the plasma mirrors).

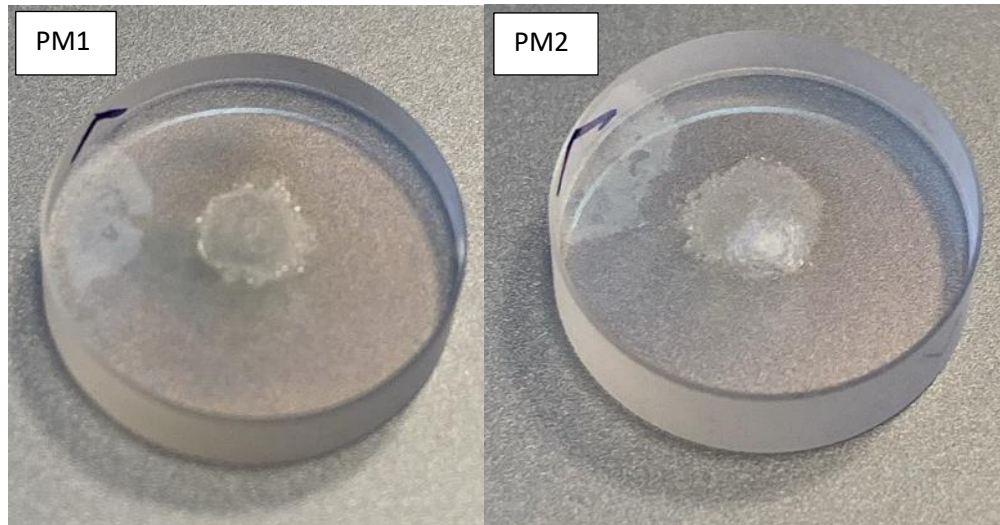


Figure S8. The laser-damaged spot size is 3.2 mm on PM1 and 3.6 mm on PM2. A larger diameter damage appears on the periphery of the mirror substrate.

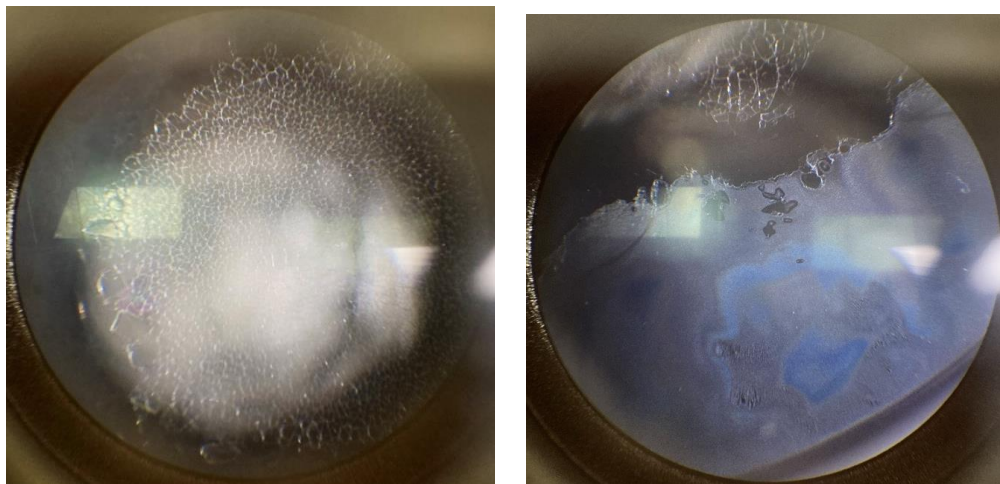


Figure S9. Left: microscope image of the surface damage at the primary beam location. The glass is shattered, and micro-cracks are created. Right: image of the secondary damage at the edge of the substrate.

Upon inspection using a microscope, the different color and the color gradients of the secondary damage area indicate that the surface was coated with a thin film of another material.

An explanation is that the plasma mirror plume of PM1 hits PM2, and plasma mirror plume of PM2 hitting PM1 as sketched in Figure S10.

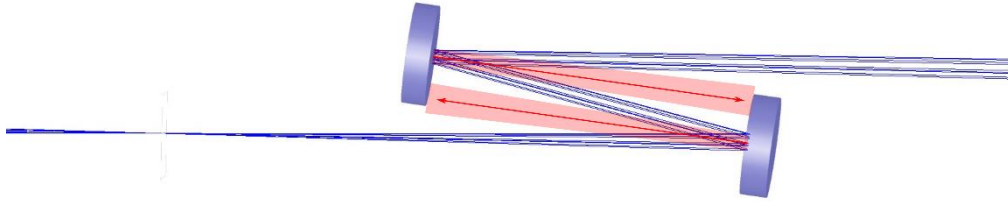


Figure S10. Plasma mirror plume from the substrate is depicted with red.

The diameter of the damage by the plasma plume is ~ 7 mm and the circle center is situated roughly at the top of PM2 and at the bottom of PM1. This implies an opening of the plasma cone of about 2 degrees. The silver layer being sputtered onto the opposite PM is well pronounced (Figure S11).

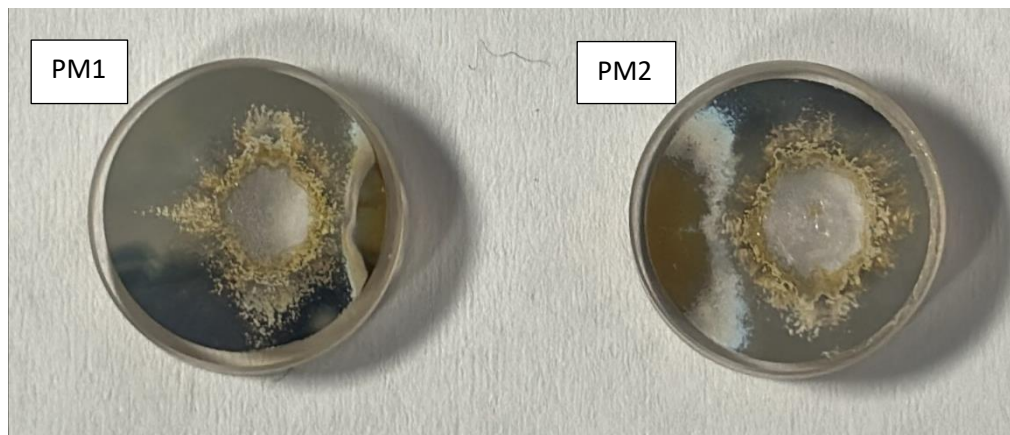


Figure S11. Image of the silver-coated DPM mirrors after shot.

3. Optomechanical design of double-plasma mirror and high-power diagnostics

The computer-aided design (CAD) of the double-plasma mirror is shown in Figure S12. Eleven double plasma mirror pairs are installed on a wheel that permits exchanging between the shots on target. The plasma mirror pairs are separated with baffles to prevent contamination of the neighbor mirror sets, as shown in Figures S8 and S11.

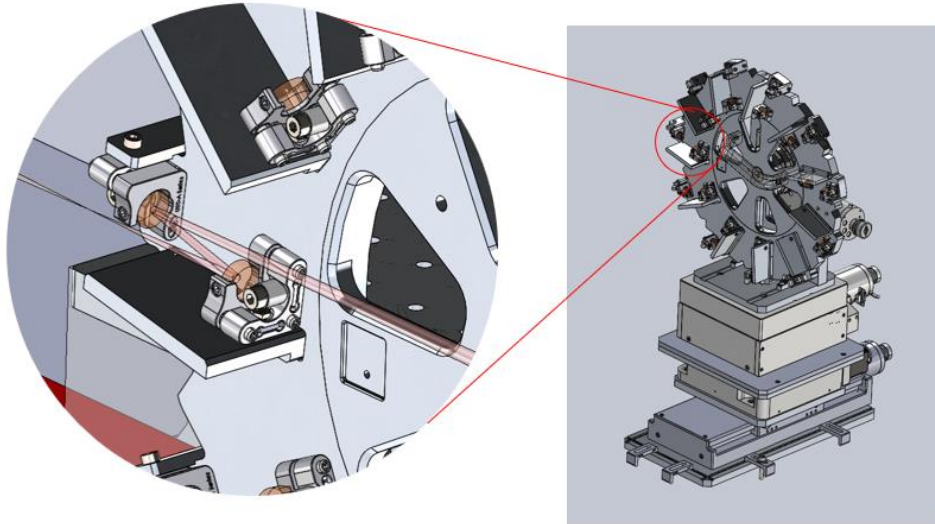


Figure S12. Mechanical implementation of the DPM wheel exchanger with two translational and two rotational axes of motion. The zoom depicts one DPM pair and the laser path towards the target chamber center. The beam is reflected in the vertical plane to ensure s-polarization of the laser on the plasma mirrors. A block is placed behind each plasma mirror to stop the transmitted light.

The complete setup of the high-power diagnostics is presented in Figure S13. M0 is a 12-inch Edmund Optics mirror substrate that is uncoated on the front (concave parabolic) surface and has an antireflecting coating (for 760-860 nm bandwidth) applied on the rear surface of the mirror. The laser beam is p-polarized on M0 impinging at 0.25° angle of incidence. The intermediate focus is imaged with a 4f relay consisting of two 1.52 m achromat lenses. The routing mirrors are silver coated, except M1, M2 and M4, which are replaced with transparent wedges to reduce the laser intensity (the beam is p-pol on the optics). The vacuum viewport has antireflective coatings for the full laser bandwidth (760-860 nm) and high optical surface quality allowing for an unperturbed transport of the beam onto the microscope table.

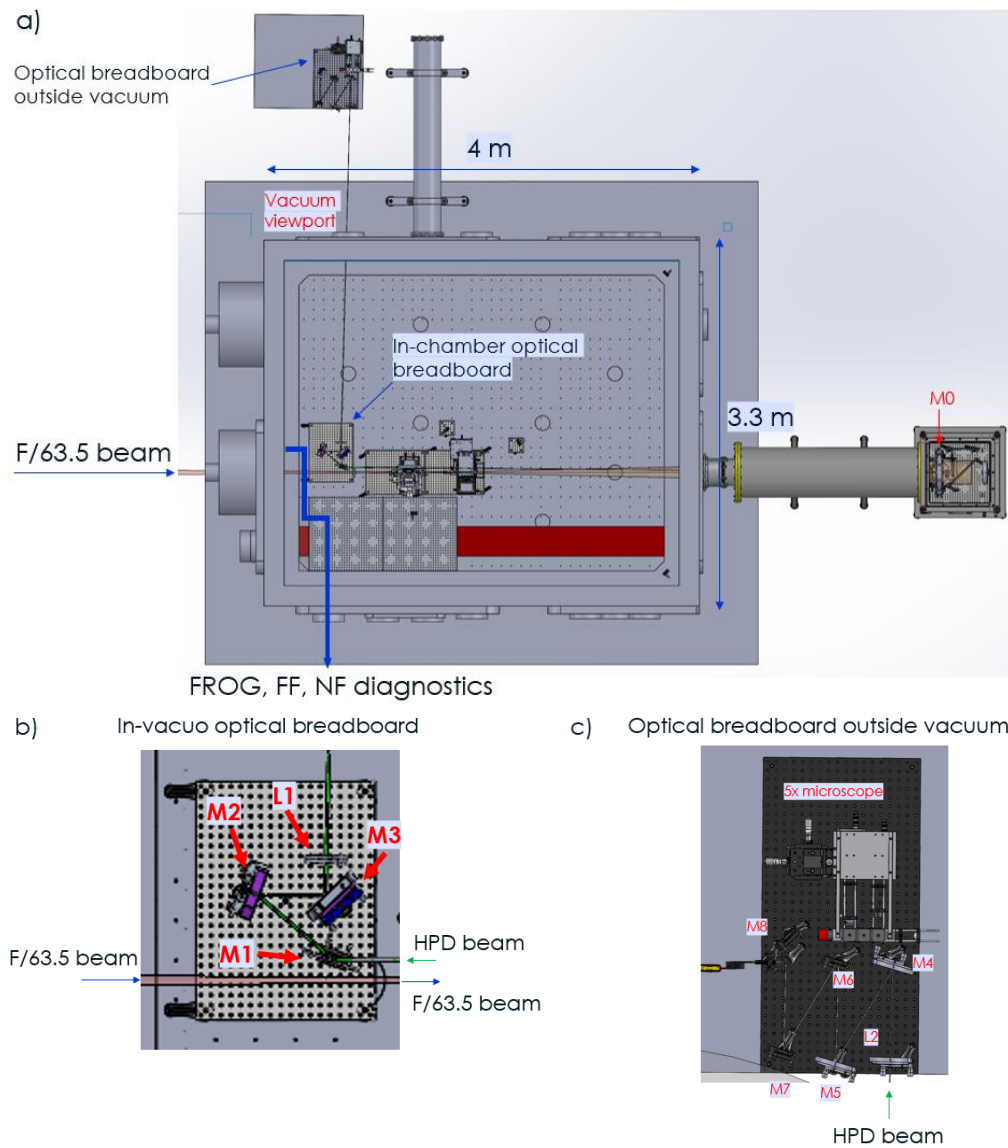


Figure S13. (a) Mechanical design of the high-power diagnostics. (b) and (c) Detailed view of the in-vacuo optical breadboard and outside vacuum chamber, respectively. Laser beam is p-polarized on the high-power diagnostic optics.

4. Background treatment in the high-power diagnostic images

Dark current on the camera is removed by subtracting an image without the laser light. An additional tilted background is derived from the four corners (100x100 pixel) of the image on shot. An example is shown in Figure S14. Background remains after simple image subtraction, as the pixel values do not oscillate around zero. A similar behavior is observed when extrapolating the mean pixel value of those corners to the full image and calculating the background contribution to the total signal.

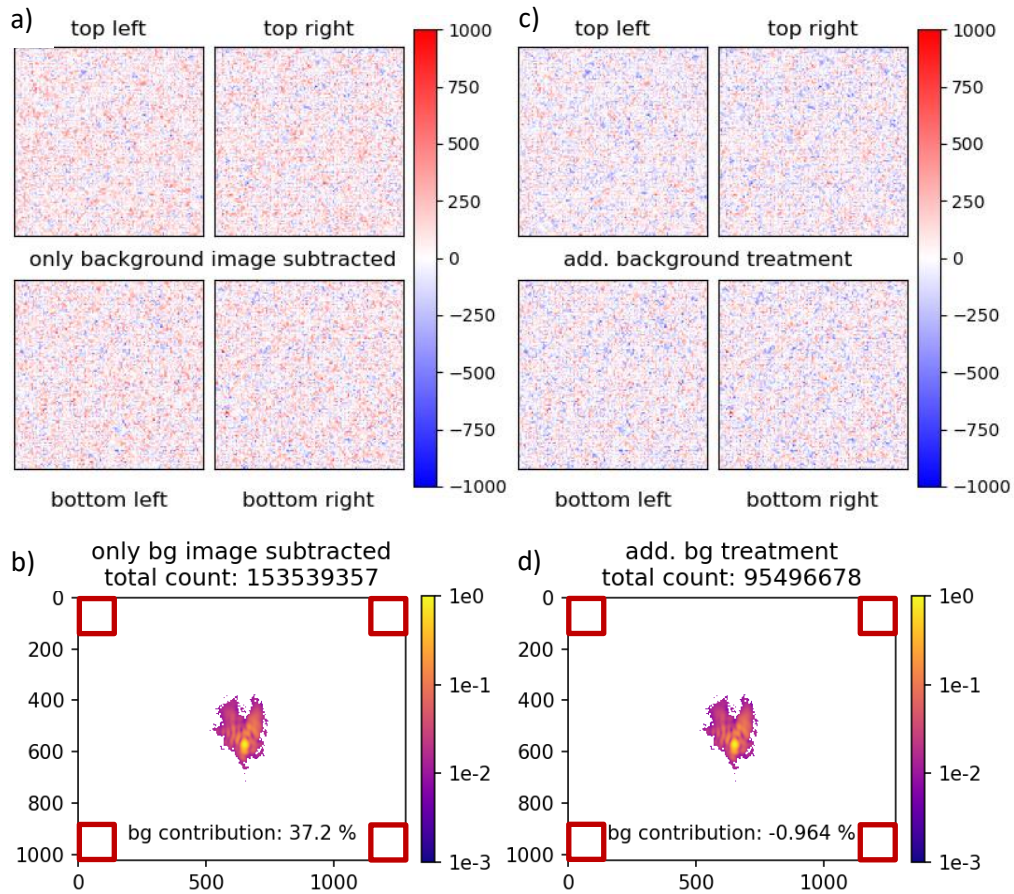


Figure S14. Comparison of the two methods of background correction. (a-b) Only the background image is subtracted. (c-d) Additional background is removed based on the extrapolation of the mean pixel values of the 4 corners of the image.

5. High-power diagnostic imaging characteristics

Imaging parameters in completion to Figure 2 are given below. The spot diagram (Figure 15a) shows that the rays from the central part of the spectrum (780-820 nm) are localized within the Airy disk, while the wavelengths at the extremities of the spectrum are the most affected by chromatic aberrations stemming from the telescope lenses. The peak-to-valley wavefront error is limited to $\lambda/5$ (Figure 15b). Modulation transfer function is given in Figure 15c. The spatial blurring is assessed with geometric image analysis (Figure 15d).

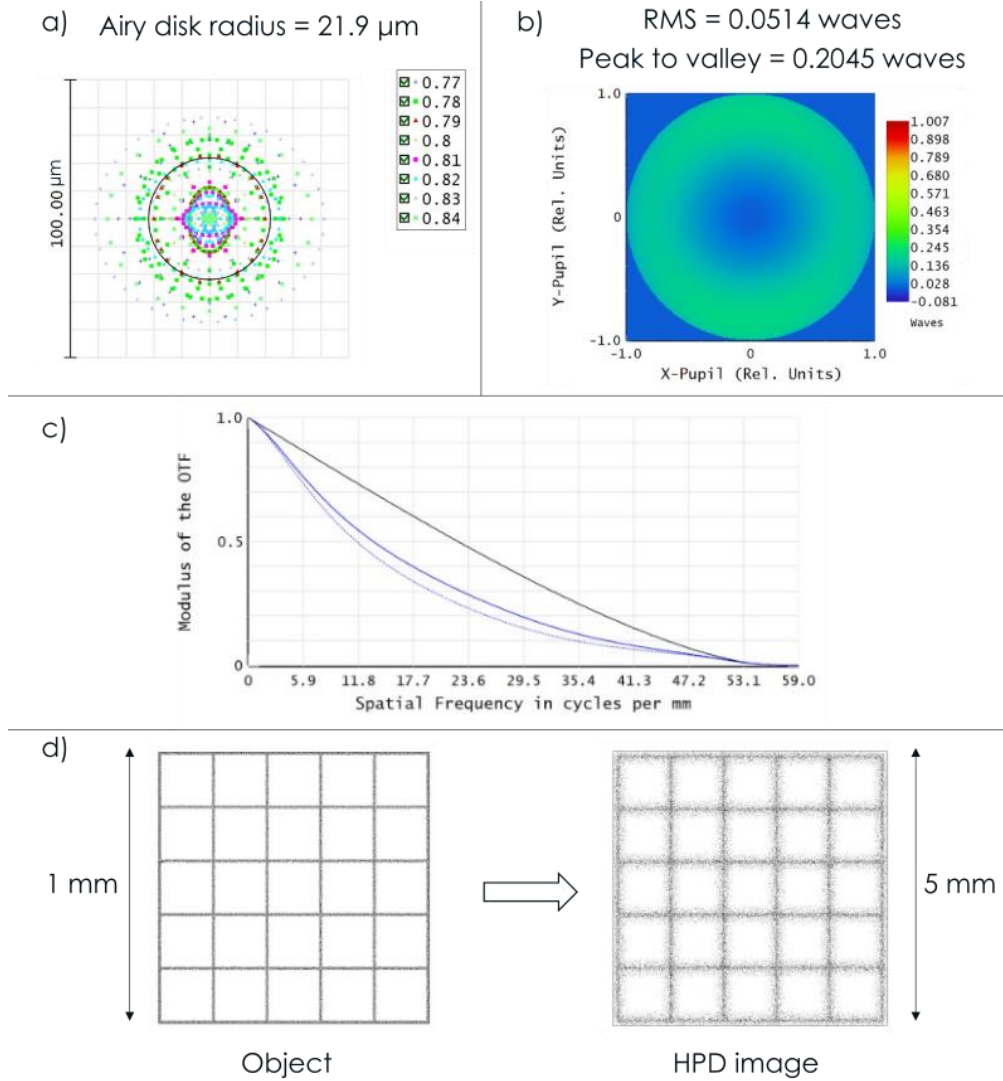


Figure S15. High-power diagnostic imaging characteristics for the demagnified focus after the DPM system. (a) Spot diagram based on rays covering the spectrum of the laser, wavelength in the legend is represented in nm. (b) Wavefront map and root-mean square deviation of the imaged focus. (c) Modulation transfer function. (d) Geometric image analysis of an object representing a 1x1 mm grid.

Seidel coefficients (Figure S16) computed for each surface give further insight into the origin of the optical aberrations of the HPD system. The sum of the aberrations clearly shows that spherical aberrations of the refocusing on-axis parabolic mirror is the dominant factor in the imaging system at the central wavelength of the laser. The spherical aberrations are well compensated in the doublet lenses of the 4-f telescope, and the chromatic aberrations are two times smaller than the spherical aberration of the refocusing mirror.

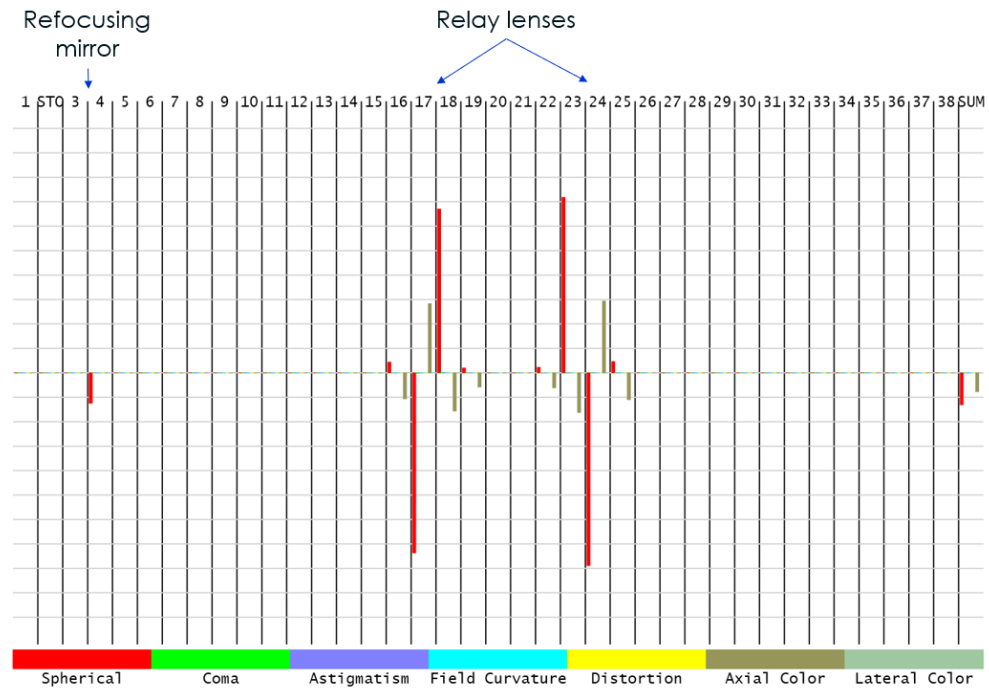


Figure S16. Seidel diagram of the HPD imaging system computed at the central wavelength of the laser 810 nm. The numbers listed at the top of the figure are the optical surfaces at which aberrations are calculated.

6. Laser pulse duration

Measurement of the laser pulse duration is done with a commercial frequency-resolved optical gating (FROG) single-shot second-order autocorrelator. The spectrum of a representative laser pulse given in Figure S17 shows the duration of the pulse that is optimized at the FROG location. The uncertainty of the pulse duration is (24 ± 1) fs.

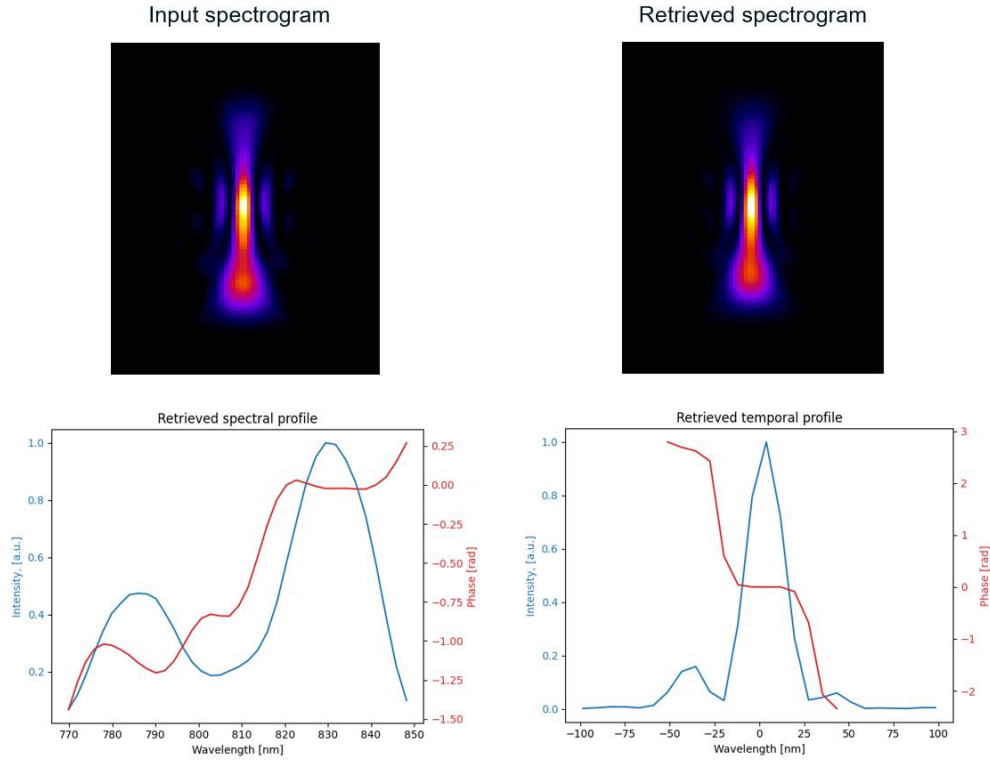


Figure S17. Retrieved duration of 24.4 fs (FWHM) for a representative laser pulse.

References

1. O. Chalus, C. Derycke, M. Charbonneau, et al., "High contrast 10 PW laser system at ELI-NP," submitted (2024).